

Superconductivity and Ferroelectric Orbital Magnetism in Semimetallic Rhombohedral Hexalayer Graphene

Jinghao Deng^{1#}, Jiabin Xie^{1#}, Hongyuan Li^{1#}, Takashi Taniguchi², Kenji Watanabe³,
Jie Shan^{4,5}, Kin Fai Mak^{1,5}, Xiaomeng Liu^{1*}

¹Laboratory of Atomic and Solid State Physics, Cornell University, Ithaca, NY, USA

²Research Center for Materials Nanoarchitectonics, National Institute for Materials Science, 1-1 Namiki, Tsukuba 305-0044, Japan

³Research Center for Electronic and Optical Materials, National Institute for Materials Science, 1-1 Namiki, Tsukuba 305-0044, Japan

⁴School of Applied and Engineering Physics, Cornell University, Ithaca, NY, USA

⁵Max Planck Institute for the Structure and Dynamics of Matter, Hamburg, Germany

[#]These authors contributed equally

*Correspondence author E-mail: xl956@cornell.edu

Abstract: Rhombohedral multilayer graphene has emerged as a promising platform for exploring correlated and topological quantum phases, enabled by its Berry-curvature-bearing flat bands. While prior work has focused on separated conduction and valence bands, we probe the extensive semimetallic regime of rhombohedral hexalayer graphene. We survey a rich phase diagram dominated by flavor-symmetry breaking and reveal an electric-field-driven band inversion through fermiology. Near this inversion, we find a superconducting-like state confined to a region with emergent electron and hole Fermi surfaces. In addition, two multiferroic orbital-magnetic phases are observed: a ferrovalley state near zero field and a ferroelectric state at large fields around charge neutrality. The latter shows electric-field-reversible magnetic hysteresis, consistent with a $\Delta P \cdot M$ multiferroic order parameter. Our fermiology analysis elucidates the correlated semimetal regime in rhombohedral graphene and underscores its potential to host diverse quantum phases.

Rhombohedral multilayer graphene has emerged as a versatile platform for exploring strongly correlated and topological quantum phases, owing to its unique flat bands with nontrivial Berry curvature^{1,2}. In the rhombohedral stacking configuration, each graphene layer is laterally displaced by one carbon-carbon bond relative to the one beneath (Fig. 1a, inset). This stacking pattern leads to strong interlayer hybridization that gaps out electronic states on the inner layers (black dots), while leaving only the top and bottom sublattices (blue and red dots) electronically active^{3,4}. As the number of layers N increases, the growing spatial separation between these active sites suppresses their hybridization, giving rise to nearly dispersionless (flat) bands at band edges. These atomic-scale flat bands greatly enhance the role of electron–electron interactions, making the system highly susceptible to a wide range of many-body instabilities. Indeed, correlated phenomena such as spontaneous symmetry breaking of spin and valley^{5–10}, superconductivity^{6,11–18}, and nematic order^{12,19} have been reported in this system.

Beyond strong correlations, the flat bands in rhombohedral graphene also carry a nonzero Berry curvature, originating from the winding of pseudospin textures. In each valley, the total Berry phase scales as $\pi N^{1,3,4}$. While time-reversal symmetry ensures cancellation of Berry phases between valleys, spontaneous valley polarization can lift this cancellation and produce orbital ferromagnetism. This mechanism underlies the recent observations of multiferroic orbital ferromagnetism¹⁰, the quantum anomalous Hall effect^{20,21}, the long-sought fractional quantum anomalous Hall state^{22,23}, and potential chiral superconductivity²⁴.

To date, most studies of rhombohedral graphene have focused on single-band phenomena under large perpendicular electric fields that open a band gap. Here, we investigate the semimetallic regime of hexalayer rhombohedral graphene, where conduction and valence bands overlap. Compared with thinner structures ($N \leq 5$), the six-layer system exhibits pronounced band overlap that creates an extended semimetallic region, while its flatter low-electric-field band dispersion amplifies correlation effects (Fig. 1c). Such two-band systems are of fundamental interest for both topology and correlations: topological insulators can arise from band inversion between orbitals^{25,26}, and interband electron-hole pairing can give rise to excitonic insulators²⁷. The tunable band overlaps of rhombohedral graphene thus provide fertile ground for correlated semimetal physics.

We report a rich phase diagram in this regime, featuring correlated insulators, superconductivity, two distinct multiferroic orbital magnetic orders, amid an intricate network of phase boundaries (Fig. 1e). Quantum oscillation fermiology reveals sweeping flavor symmetry breaking, links the phase boundaries to multiple Lifshitz transitions of the two-flavor band structure, and uncovers a band inversion in one flavor as the electric field is tuned. Between this band inversion and a multiferroic phase, we identify two emergent Fermi surfaces; where they overlap, we find evidence for superconductivity with an in-plane critical field exceeding the Pauli limit by more than an order of magnitude. Between the correlated and band insulator, we uncover an orbital magnet with electric and magnetic hysteresis. Strikingly, the polarity of the magnetic hysteresis can be reversed by the electric field, signaling an intertwined electric-magnetic order. Our understanding of symmetry breaking and Lifshitz transitions in this system, established through detailed quantum oscillation fermiology, can guide future exploration of higher N rhombohedral graphene.

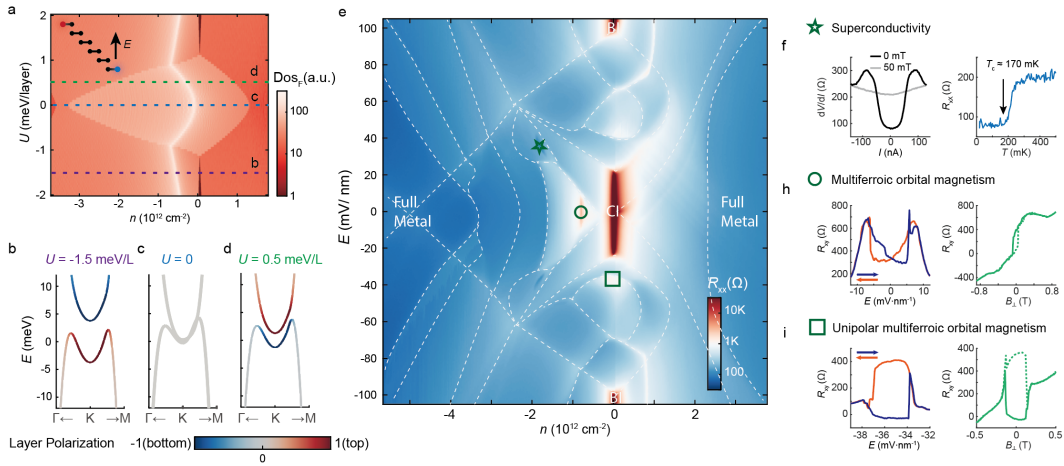


Figure 1 | Band structure and phenomenology of semimetallic rhombohedral hexalayer graphene.

a, Density of states at the Fermi energy vs carrier density n and interlayer potential U , from a tight-binding calculation. The spindle-shaped pink region indicates simultaneous intersection of the Fermi energy with conduction and valence bands. Inset, schematic of the rhombohedral six-layer structure, with active sublattices highlighted in blue and red. **b**, Band structure near the K point for three U values marked in **a**, with line color denoting layer polarization. **c**, Band structure for $U = 0$. **d**, Band structure for $U = 0.5 \text{ meV/L}$. **e**, Longitudinal resistance vs n and perpendicular electric field E (pointing upward). Major features are outlined with dashed lines; BI and CI denote band and correlated insulators. Symbols mark locations of selected quantum phases. **f**, Superconductivity signatures, including a magnetic-field-sensitive differential-resistance gap and a sharp resistivity drop near 170 mK. **g**, Ferrovalley orbital magnetism in the triangular region around $E=0$, switchable by electric and magnetic fields. **i**, Ferroelectric orbital ferromagnetism with a unipolar electric-field hysteresis loop.

We first review the single particle bands. Figure 1a shows the calculated density of states at the Fermi energy (DOS_F) as a function of carrier density and interlayer potential U , obtained from a tight-binding model. U represents the onsite potential difference between adjacent layers and is equivalent to the experimentally applied perpendicular electric field E . At $U = 0$ (Fig. 1c), the electron and hole bands overlap significantly, with the corresponding wavefunction equally distributed between the top and bottom layers. Applying a finite electric field breaks this symmetry, leading to layer-polarized states at the band edges, with the polarization direction depending on the field orientation (Figs. 1b & 1d). As the field increases, the potential further separates the conduction and valence bands and produces a band gap (Fig. 1d). Across electric fields, the conduction band is approximately a parabola while the valence band is shaped as an inverted Mexican hat.

Figure 1e shows experimental four-terminal longitudinal resistance (on a logarithmic scale) as a function of carrier density n and perpendicular electric field E (pointing upwards). Consistent with the calculated density of states at the Fermi level in Fig. 1a, a transport gap opens at charge neutrality once the electric field exceeds a threshold of approximately 100 mV/nm. Below this threshold, a rich landscape of phase boundaries (delineated by dashed lines) and quantum phases unfolds in the single particle semimetal regime.

At charge neutrality near zero electric field, situate the correlated insulator (CI, temperature dependence shown in Fig. S1). Slight hole doping brings a triangular region that hosts ferrovalley orbital ferromagnetism, characterized by hysteretic Hall response in magnetic and electric fields (Fig. 1h, more in Fig. S2), similar to those seen in pentalayer rhombohedral graphene¹⁰. A region at the tail of this triangle holds a superconducting-like phase (SC1). Although the resistance does not reach zero, its temperature, magnetic field, and current dependence are consistent with superconductivity or a fragile superconductor (Fig. 1f). Around $n = 0$ and $E \approx -35$ mV/nm, we identify a second multiferroic orbital ferromagnetic phase that exhibits unipolar switching behavior in the electric field (Fig. 1i). That is, both forward and backward switching is offset in the same electric field direction (~ -34 mV/nm and ~ -37 mV/nm, respectively).

Understanding the correlated insulator is central to interpreting the phase diagram. At $E = 0$, single-particle theory predicts wavefunctions as equal-weight superpositions of the top and bottom layers (Fig. 1c). Electron interactions, however, drive pseudospin ferromagnetism that produces spontaneous layer polarization and opens an emergent gap²⁸. This polarization can orient upward or downward, effectively mimicking a positive or negative external electric field, which we refer to as a positive or negative emergent gap.

In rhombohedral graphene, a uniform emergent gap across spin and valley would place all four bands in the same layer, incurring a large Coulomb penalty. At $E = 0$, the energetically favored state instead adopts a two-by-two splitting: two isospins acquire positive emergent gaps and the other two acquire negative ones, thereby forming two flavored bands (Fig. 2j). The specific flavor pairing determines the broken symmetry—spin, valley, or a mixed combination. The commonly recognized layer antiferromagnetism corresponds to spin splitting, where spin-up and spin-down experience opposite emergent fields and occupy opposite layers^{2,8,18,29,30}. Alternatively, an inter-valley coherent insulator can arise from superpositions of the K and K' valleys with the canceling Berry phase^{31,32}. Without the ability to distinguish them, we refer to the two flavored bands, each two-fold degenerate, generically as flavor A (negative emergent gap) and B (positive emergent gap).

With increasing electric field, the gap at flavor A shrinks while that of flavor B expands, reflecting the lowering (raising) of potential energy in the bottom (top) layer (Fig. 2i&j). At larger fields, the gap at flavor A closes and inverts from negative to positive (Fig. 2g&h). As we show below, many of the phase boundaries in Fig. 1e can be understood in connection with this flavor-broken band inversion.

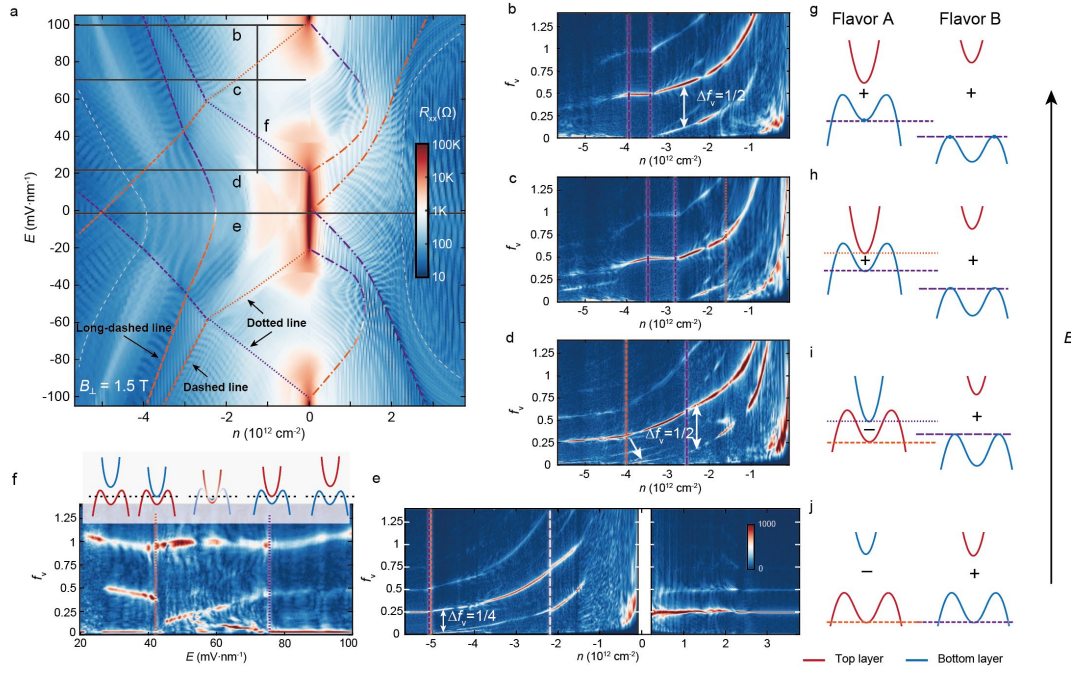


Figure 2 | Fermiology of symmetry-breaking semimetal.

a, Longitudinal resistance vs n and E at 1.5 T. Purple and orange lines mark phase boundaries associated with the discussed Lifshitz transitions, with colors reflecting the inferred layer polarization of the corresponding band. **b–e**, Fourier transform of $R_{xx}(1/B)$ vs n and normalized frequency along the electric-field line cuts indicated in **a**. Vertical purple and orange lines denote quantum-oscillation changes corresponding to a Lifshitz transition, aligned with the phase boundaries in **a**. **f**, Quantum-oscillation map vs E along the vertical cut in **a**, with the band diagram above showing the corresponding evolution of flavor A. Black dotted lines represent the Fermi energy. **g–j**, Band diagrams at various electric fields matching **b–e**. Dotted and dashed lines indicate Fermi levels at the Lifshitz transitions, with line patterns consistent with previous panels.

In Fig. 2a, we show the longitudinal resistance under a perpendicular magnetic field of 1.5 T. Sudden changes in the quantum oscillations occur along the orange and purple boundaries, which we identify as Lifshitz transitions. These phase boundaries form a subset of those in Fig. 1e. Here we focus on the hole-doped side, while the electron-doped fermiology is presented in Fig. S3. Figs. 2b–f show the fast Fourier transform (FFT) of quantum oscillation along horizontal and vertical line cuts of Fig. 2a (raw data are shown in Figs. S4). The vertical axis in these panels, f_v , is defined as the normalized oscillation frequency: $f_v = f_{FFT} \cdot e/nh$, where f_{FFT} is the oscillation frequency of $R_{xx}(1/B_{\perp})$, and e , n , and h are the electron charge, carrier density, and Planck’s constant, respectively. Physically, f_v represents the number of Bloch states enclosed by the Fermi surface relative to the carrier density. For a simple, non-degenerate parabolic band, f_v peaks at 1, while double degenerate parabolic bands produce a peak at 0.5.

In Fig. 2b, to the right of the purple dashed line, two dominant oscillation frequencies appear, separated by 0.5 in f_v , indicating an annular Fermi surface with two-fold degeneracy. This observation illustrates that doping the band insulator creates symmetry-breaking metal, consistent with flavored bands in Fig. 2g. The lower-frequency branch vanishes at the dashed purple line, signaling the disappearance of the inner circle of the annular Fermi surface. Below this line, the Fermi surface becomes simply connected, giving rise to a peak fixed at $f_v = 0.5$. As hole doping increases further, the Fermi energy drops to the band edge of flavor B—marked by the long dashed purple line in Figs. 2b and 2g—entering a regime of partial flavor polarization (where the sum rule of f_v is violated, discussion of the sum rule is presented in Fig. S5).

At reduced electric field, Fig. 2c shows the same phase boundaries (purple dashed lines), shifted in the positive n direction. This reflects an upward energy shift in the corresponding band features with decreasing electric field, consistent with bottom-layer polarization. This trend is also evident in the backward tilt of the purple lines in the n - E map of Fig. 2a. Additionally, a new electron pocket

emerges in Fig. 2c and vanishes near $n \sim -1.5 \times 10^{12} \text{ cm}^{-2}$, bounded by the dotted orange line. The appearance of these electron pockets at negative n corroborates the band overlap between conduction and valence bands. The dotted orange line marks the conduction band edge (Fig. 2h), and its tilt opposite in the n - E map (Fig. 2a) to the purple lines indicates top-layer polarization. Accordingly, we associate purple lines with bottom-layer band features and orange lines with top-layer polarized bands.

As the electric field lowers further ($< 60 \text{ mV/nm}$), we identify similar phase boundaries, marked by orange dashed lines and purple dotted lines, corresponding to the valence band minimum and conduction band edge (white arrow in Fig. 2d and f_3 Fig. S5i). Yet, the energy evolution of these boundaries in the electric field is opposite to that of $E > 60 \text{ mV/nm}$, evident from their line tilts in Fig. 2a. This indicates an inversion between conduction band edge (dotted line) and valence band bottom (dashed line) as shown in flavor A in Fig. 2h&i.

An electric-field line cut at $n = -1.26 \times 10^{12} \text{ cm}^{-2}$ captures the inversion process (Fig. 2f). To the right of the dotted purple line, we observe annular Fermi surfaces polarized to the bottom layer. As E decreases past the purple boundary ($\sim 75 \text{ mV/nm}$), a top-layer-polarized electron Fermi surface emerges. With further reduction of E , this top-layer surface expands while the bottom-layer surface shrinks, consistent with their relative potential shifts (Fig. 2f, upper inset). At $E \sim 42 \text{ mV/nm}$, the two Fermi surfaces cross; below this point, the bottom-layer polarized band becomes the electron band and rises above the Fermi level at the dotted orange line. The band inversion is then complete, leaving a top-layer-polarized valence band.

Most boundaries in Fig. 1e can be understood by such an E -dependent but n -independent band picture. However, notable exceptions arise. At large electron and hole doping (grey dashed lines in Fig. 2a), the bands regain fourfold degeneracy (Fig. 2d&e). More puzzling is the observation at $E = 0$: to the right of the long-dashed white line in Fig. 2e, the annular Fermi surfaces are only two-fold degenerate, in contrast to the band picture of Fig. 2j, which predicts fourfold degenerate bands at $E = 0$. Equally striking, the valley-polarized orbital magnetism in the triangular region is incompatible with the widely assumed layer antiferromagnet at charge neutrality under the same electric field^{8,30}. Together, these anomalies suggest either evolution of the correlated band upon doping or a ground state with an alternative flavor polarization.

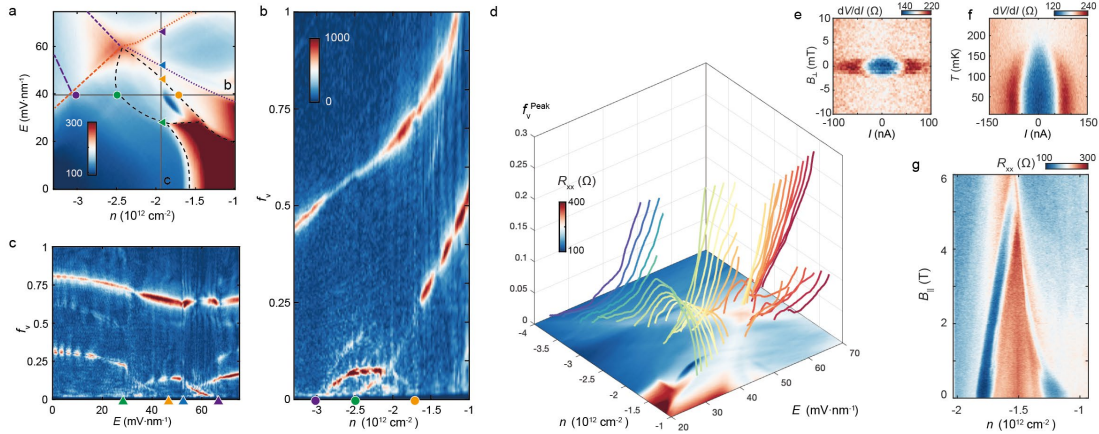


Figure 3 | Emergent Fermi surface and superconductivity.

a, Longitudinal resistance in a narrow n - E region near band inversion. **b&c**, Fermiology along the horizontal and vertical grey lines in **a**; dots and triangles mark f_i peaks reaching zero frequency, with corresponding n - E positions indicated in **a**. **d**, 3D evolution of f_i peaks overlaid on the resistance map. **e**, Differential resistance vs current and magnetic field at base temperature. **f**, Differential resistance vs current and temperature at zero field. **g**, In-plane field dependence of longitudinal resistance along a line cut through two superconducting phases (see Fig. S12a); the main phase corresponds to the left blue strip.

Most interestingly, we observe an intriguing Fermi surface reconstruction around the intersection of the purple and orange dashed and dotted lines, where the bands in flavor A are inverted. Figure

3a highlights the intricate features in this region. Between the multiferroic triangle (bottom right) and the band crossing intersection, faint features in R_{xx} , outlined by black dashed lines, encircle an area that resembles a leaf.

Figures 3b and 3c present quantum oscillation fermiology along horizontal and vertical line cuts across the leaf-shaped region (cut positions indicated by solid grey lines in Fig. 3a). In Fig. 3b, a Fermi surface (which we refer as FS1) emerges as n reaches the purple dot, grows with increasing n , and then decreases and disappears near the orange dot—forming an arc. Such evolution is incompatible with an n -independent band structure, as it implies the Fermi energy traverses an isolated band. Inside this arc, a separate electron-like Fermi surface emerges near the green dot, which we call FS2. The higher f_v peak exceeds the sum of FS1 and FS2 by 0.5, indicating two-fold-degenerate Fermi surfaces (Fig. S5). Notably, FS1 and FS2 disappear rapidly with increasing temperature, underscoring their emergent nature (Fig. S6). In the fixed n linecut of Fig. 3c, a separate arc-shaped feature spans the green and purple triangles, with additional Fermi surface terminations occurring at the yellow and green triangles. This evolution with E resembles two successive band crossings, each analogous to the scenario shown in Fig. 2f.

To clarify the relationship between resistance features and fermiology, we mark positions of Lifshitz transitions, as identified from Figs. 3b and 3c, in Fig. 3a with corresponding symbols. These symbols notably align with marked phase boundaries. To further trace the evolution of the Fermi surfaces, we extract f_v peaks from a series of fermiology measurements along multiple E -field cuts and overlay them on the resistance map in Fig. 3d, focusing on the low f_v region (FFT results are shown in Figs. S7 and S8, along with extracted peak positions). We find that as E increases above ~ 30 meV/nm and enters the leaf-shaped region, the inner pocket of the annular Fermi surface splits into FS1 and FS2. It is also clear from Fig. 3d that these f_v peaks belong to three manifolds, one half-dome stretching from the orange dashed line to the right edge of the leaf, one from the left leaf boundary to the orange dotted line, and the last one intersecting the purple dashed line and purple dotted line.

Within the leaf-shaped region lies the previously identified superconducting-like state, characterized by an onset temperature of approximately 170 mK (Figs. 1f and 3f). In addition to a sharp drop in resistance, the differential conductance (dV/dI) exhibits characteristic features of superconductivity. As shown in Fig. 3e, these features are suppressed by a small out-of-plane magnetic field. Notably, the low-resistance state persists up to an in-plane magnetic field of approximately 6 T—more than an order of magnitude higher than the estimated Pauli limit of ~ 300 mT based on the observed T_c (see Fig. S9 for resistance n - E maps at various in-plane magnetic fields). While the resistance does not reach zero, this may be due to insufficient filtering, or it could suggest a fragile superconductivity. The confinement of this state strictly within the leaf-shaped region, where the two emergent Fermi surfaces overlap, hints at a possible dual carrier origin.

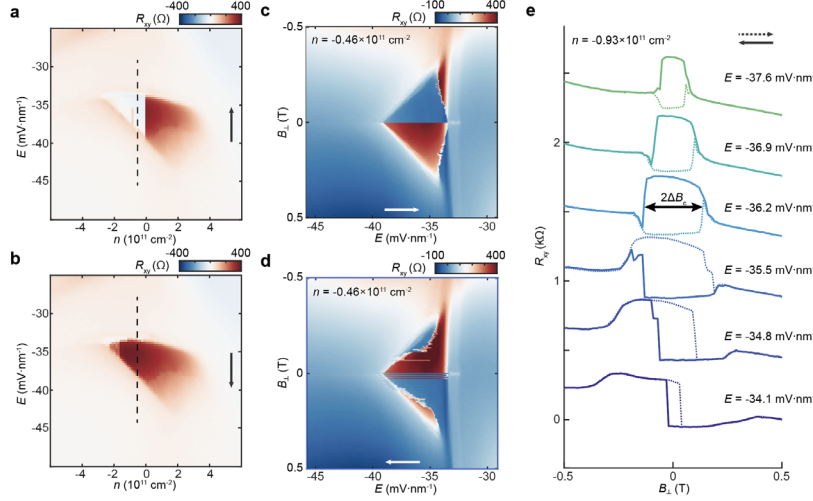


Figure 4 | Ferroelectric orbital magnetism.

a&b, Hall resistance in a small n - E area around the green square mark of Fig. 1e under a small magnetic field of $B_{\perp} = 50$ mT. The fast scan direction is indicated by the arrow inside each panel. **c&d**, Electric field hysteresis vs perpendicular magnetic fields. The direction of scanning is indicated by white arrows. **e**, Magnetic field hysteresis vs E , with dashed (solid) lines plotting forward (backward) scan.

We last discuss a novel multiferroic order near $n = 0$ at finite E , which exhibits characteristics distinct from the multiferroic phase around $E = 0$ in the triangular region (Fig. S2). This order appears in a comet-shaped region of the n - E phase space. On the left of this comet, a pronounced hysteresis in Hall resistance R_{xy} is observed when sweeping the electric field forward and backward under a small stabilizing perpendicular magnetic field of 50 mT (Fig. 4a,b). The sign of the electric-field hysteresis reverses as B_{\perp} changes sign, while the size of the hysteresis loop shrinks linearly with increasing B_{\perp} magnitude (Fig. 4c,d). The step-like R_{xy} vs E (Fig. 1i) differs qualitatively from the butterfly-shaped E -hysteresis seen in the triangle region (Fig. 1h) and in pentalayer graphene¹⁰. We refer to the butterfly-shaped hysteresis as ferrovalley orbital magnetism, due to the absence of electric dipole and Berry curvature at $E = 0$, and the step-like hysteresis as ferroelectric orbital magnetism. On the right end of the comet, the anomalous Hall effect remains, but without hysteresis in either magnetic or electric field response (Fig. S10). Temperature-dependent measurements reveal the characteristic temperature of the multiferroic behavior of $T_c = 1.5$ K (Fig. S11).

The magnetic-field dependence of R_{xy} is more striking. As the electric field is tuned at a fixed $n = -0.93 \times 10^{11} \text{ cm}^{-2}$, the magnetic hysteresis changes sign: for $E \geq -35.5$ mV/nm, forward B -field sweeps (dashed lines) yield higher R_{xy} than backward sweeps (solid lines), whereas for $E \leq -36.2$ mV/nm the opposite is true. This sudden transition happens when the magnetic hysteresis is the largest. In previously reported pentalayer multiferroicity, the magnetic hysteresis direction is insensitive to E ¹⁰. Since R_{xy} reflects the orbital magnetization, E -controlled magnetic hysteresis polarity indicates that $M \cdot B$ alone does not capture the system's energetics and points to multiferroicity with order parameter $\Delta P \cdot M$, where P is the electric polarization.

The microscopic origin of the hysteretic electric dipole remains unclear. One possible scenario is that a 3:1 polarized state with three positive (negative) emergent gaps and one negative (positive) emergent gap among the four isospins. This is consistent with its position in the phase diagram, between the fully layer-polarized band insulator and the layer-unpolarized correlated insulator. An additional superconducting-like feature (SC2) appears in the nearby region of the ferroelectric orbital magnetism (Fig. S12). Because both multiferroic order is accompanied by a superconducting state, we note a potential connection between these phases.

Methods

Device preparations. The hexalayer graphene and hBN flakes were prepared by mechanical exfoliation of high-quality graphite and hBN single crystal onto SiO₂/Si substrates. SiO₂/Si substrates are oxygen-plasma treated before graphene exfoliation to elevate the yield of rhombohedral graphene layers. The rhombohedral domains were identified by using Raman spectroscopy with a 532 nm laser at room temperature³³ and then isolated by anodic oxidation lithography with atomic force microscope (see Fig. S13)³⁴. Our heterostructure was assembled with a dry transfer technique³⁵ using poly(bisphenol A carbonate)/polydimethylsiloxane stamp. We use the following sequence for pickup: graphite (top gate)/hBN/rhombohedral graphene/hBN/graphite (bottom gate). After assembling all the layers, we release the stacks on SiO₂/Si chips. The geometry of the Hall bar devices was defined by combining CHF₃/O₂ and O₂ etching. After Hall bar etching, we deposit Cr(5 nm)/Pd(15 nm)/Au(80 nm) as contacts to the rhombohedral graphene³⁵. For better contact, we performed another etching by CHF₃/O₂ plasma right before metal evaporation. Three devices were fabricated and measured with similar results.

Transport measurements. The devices were studied in an Oxford Proteox dilution refrigerator with a base temperature of 9 mK. Stanford SR860 lock-in amplifiers were used for DC transport measurements with the frequency ranging from 17.777 to 37.777 Hz. We measure longitudinal four-terminal voltages, bias currents, and Hall voltages simultaneously to obtain R_{xx} and R_{xy} . For current dependent dI/dI measurements, we use a Keithley 2450 with a 4.7 M Ω serial resistance to generate DC current bias. For better electrical contact, we apply voltages to the global silicon gate ranging from -90 to -100 V in the hole-doping side, and 95 V for the electron side.

Tight-binding calculations. The single-particle band structure of rhombohedral hexalayer graphene was calculated using a tight-binding model for the 2N-band continuum Hamiltonian, with parameters taken from previous literature^{4,36}.

An interlayer potential difference was modelled as a layer-dependent on-site energy shift δ , varied to simulate the effect of a perpendicular electric field. For each δ , the Hamiltonian was diagonalized on a uniform triangular grid of k -points in the irreducible Brillouin zone, and the density of states was computed from the histogram of all eigenvalues. Repeating this procedure over a range of δ produced the two-dimensional map DOS(E , δ). Layer polarization shown in Fig. 1b is defined as $|\psi_{\text{top}}|^2 - |\psi_{\text{bot}}|^2 / (|\psi_{\text{top}}|^2 + |\psi_{\text{bot}}|^2)$.

Acknowledgments

We acknowledge helpful discussions with C. Chang, J. Zhu, T. Cao, M. Yankowitz, C. Lewandowski, D. Chowdhury, and C. Jian. X. L. acknowledges support from the National Science Foundation through the CAREER program under Award No. DMR-2442363. J. D. acknowledges support from the New Frontier Grant, College of Arts & Sciences, Cornell University. The device fabrication is performed in part in Cornell Center for Materials Research and in part at the Cornell NanoScale Facility, a member of the National Nanotechnology Coordinated Infrastructure (NNCI), which is supported by the National Science Foundation (Grant NNCI-2025233). K.W. and T.T. acknowledge support from the JSPS KAKENHI (Grant Numbers 21H05233 and 23H02052), the CREST (JPMJCR24A5), JST and World Premier International Research Center Initiative (WPI), MEXT, Japan.

Author Contributions

J. D., J. X., H. L., and X. L. conceived the project. J. D., J. X., and H. L. fabricated the device. J. D. performed the transport measurement and analyzed the data with the help of H. L. and J. X. K.W. and T. T. provided hBN crystals. X. L. supervised the project and provided input on data analysis. J. D. and X.L. wrote the manuscript with input from all authors.

Competing interests

The authors declare no competing interests.

Additional information

Supplementary information is available for this paper at XXX.

Reference

1. Xiao, D., Chang, M.-C. & Niu, Q. Berry phase effects on electronic properties. *Rev. Mod. Phys.* **82**, 1959–2007 (2010).
2. Zhang, F., Jung, J., Fiete, G. A., Niu, Q. & MacDonald, A. H. Spontaneous Quantum Hall States in Chirally Stacked Few-Layer Graphene Systems. *Phys. Rev. Lett.* **106**, 156801 (2011).
3. Min, H., Borghi, G., Polini, M. & MacDonald, A. H. Pseudospin magnetism in graphene. *Phys. Rev. B* **77**, 041407 (2008).
4. Zhang, F., Sahu, B., Min, H. & MacDonald, A. H. Band structure of ABC-stacked graphene trilayers. *Phys. Rev. B* **82**, 035409 (2010).
5. Zhou, H. *et al.* Half- and quarter-metals in rhombohedral trilayer graphene. *Nature* **598**, 429–433 (2021).
6. Zhou, H. *et al.* Isospin magnetism and spin-polarized superconductivity in Bernal bilayer graphene. *Science* **375**, 774–778 (2022).
7. Han, T. *et al.* Correlated insulator and Chern insulators in pentalayer rhombohedral-stacked graphene. *Nat. Nanotechnol.* **19**, 181–187 (2024).
8. Liu, K. *et al.* Spontaneous broken-symmetry insulator and metals in tetralayer rhombohedral graphene. *Nat. Nanotechnol.* **19**, 188–195 (2024).
9. Sha, Y. *et al.* Observation of a Chern insulator in crystalline ABCA-tetralayer graphene with spin-orbit coupling. *Science* **384**, 414–419 (2024).
10. Han, T. *et al.* Orbital multiferroicity in pentalayer rhombohedral graphene. *Nature* **623**, 41–47 (2023).
11. Zhou, H., Xie, T., Taniguchi, T., Watanabe, K. & Young, A. F. Superconductivity in rhombohedral trilayer graphene. *Nature* **598**, 434–438 (2021).
12. Holleis, L. *et al.* Nematicity and orbital depairing in superconducting Bernal bilayer graphene. *Nat. Phys.* **21**, 444–450 (2025).
13. Zhang, Y. *et al.* Twist-programmable superconductivity in spin-orbit-coupled bilayer graphene. *Nature* **641**, 625–631 (2025).
14. Patterson, C. L. *et al.* Superconductivity and spin canting in spin-orbit-coupled trilayer graphene. *Nature* **641**, 632–638 (2025).
15. Kumar, M. *et al.* Superconductivity from dual-surface carriers in rhombohedral graphene. Preprint at <https://doi.org/10.48550/arXiv.2507.18598> (2025).
16. Morissette, E. *et al.* Superconductivity, Anomalous Hall Effect, and Stripe Order in Rhombohedral Hexalayer Graphene. Preprint at <https://doi.org/10.48550/arXiv.2504.05129> (2025).
17. Li, C. *et al.* Tunable superconductivity in electron- and hole-doped Bernal bilayer graphene. *Nature* **631**, 300–306 (2024).
18. Choi, Y. *et al.* Superconductivity and quantized anomalous Hall effect in rhombohedral graphene. *Nature* **639**, 342–347 (2025).
19. Morissette, E., Qin, P., Watanabe, K., Taniguchi, T. & Li, J. I. A. Coulomb-driven Momentum Space Condensation in Rhombohedral Hexalayer Graphene. Preprint at <https://doi.org/10.48550/arXiv.2503.09954> (2025).
20. Han, T. *et al.* Large quantum anomalous Hall effect in spin-orbit proximitized rhombohedral graphene. *Science* **384**, 647–651 (2024).
21. Lu, Z. *et al.* Extended quantum anomalous Hall states in graphene/hBN moiré superlattices. *Nature* **637**, 1090–1095 (2025).
22. Xie, J. *et al.* Tunable Fractional Chern Insulators in Rhombohedral Graphene Superlattices. Preprint at <https://doi.org/10.48550/arXiv.2405.16944> (2025).
23. Lu, Z. *et al.* Fractional quantum anomalous Hall effect in multilayer graphene. *Nature* **626**, 759–764 (2024).

24. Han, T. *et al.* Signatures of chiral superconductivity in rhombohedral graphene. *Nature* **643**, 654–661 (2025).
25. Bernevig, B. A., Hughes, T. L. & Zhang, S.-C. Quantum Spin Hall Effect and Topological Phase Transition in HgTe Quantum Wells. *Science* **314**, 1757–1761 (2006).
26. König, M. *et al.* Quantum Spin Hall Insulator State in HgTe Quantum Wells. *Science* **318**, 766–770 (2007).
27. Jérôme, D., Rice, T. M. & Kohn, W. Excitonic Insulator. *Phys. Rev.* **158**, 462–475 (1967).
28. MacDonald, A. H., Jung, J. & Zhang, F. Pseudospin order in monolayer, bilayer and double-layer graphene. *Phys. Scr.* **2012**, 014012 (2012).
29. Weitz, R. T., Allen, M. T., Feldman, B. E., Martin, J. & Yacoby, A. Broken-Symmetry States in Doubly Gated Suspended Bilayer Graphene. *Science* **330**, 812–816 (2010).
30. Shi, Y. *et al.* Electronic phase separation in multilayer rhombohedral graphite. *Nature* **584**, 210–214 (2020).
31. Liao, W.-Y. *et al.* Intervalley Coherent Order in Rhombohedral Tetralayer Graphene on MoS₂. *Phys. Rev. Lett.* **135**, 046202 (2025).
32. Liu, Y. *et al.* Visualizing incommensurate inter-valley coherent states in rhombohedral trilayer graphene. Preprint at <https://doi.org/10.48550/arXiv.2411.11163> (2024).
33. Lui, C. H. *et al.* Imaging Stacking Order in Few-Layer Graphene. *Nano Lett.* **11**, 164–169 (2011).
34. Li, H. *et al.* Electrode-Free Anodic Oxidation Nanolithography of Low-Dimensional Materials. *Nano Lett.* **18**, 8011–8015 (2018).
35. Wang, L. *et al.* One-Dimensional Electrical Contact to a Two-Dimensional Material. *Science* **342**, 614–617 (2013).
36. Dong, J. *et al.* Anomalous Hall Crystals in Rhombohedral Multilayer Graphene. I. Interaction-Driven Chern Bands and Fractional Quantum Hall States at Zero Magnetic Field. *Phys. Rev. Lett.* **133**, 206503 (2024).

Supplementary Information for:

**Superconductivity and Ferroelectric Orbital Magnetism in
Semimetallic Rhombohedral Hexalayer Graphene**

Jinghao Deng^{1#}, Jiabin Xie^{1#}, Hongyuan Li^{1#}, Takashi Taniguchi², Kenji Watanabe³, Jie Shan^{4,5}, Kin Fai Mak^{1,5}, Xiaomeng Liu^{1}*

¹Laboratory of Atomic and Solid State Physics, Cornell University, Ithaca, NY, USA

²Research Center for Materials Nanoarchitectonics, National Institute for Materials Science, 1-1 Namiki, Tsukuba 305-0044, Japan

³Research Center for Electronic and Optical Materials, National Institute for Materials Science, 1-1 Namiki, Tsukuba 305-0044, Japan

⁴School of Applied and Engineering Physics, Cornell University, Ithaca, NY, USA

⁵Max Planck Institute for the Structure and Dynamics of Matter, Hamburg, Germany

[#]These authors contributed equally

**Correspondence author E-mail: xl956@cornell.edu*

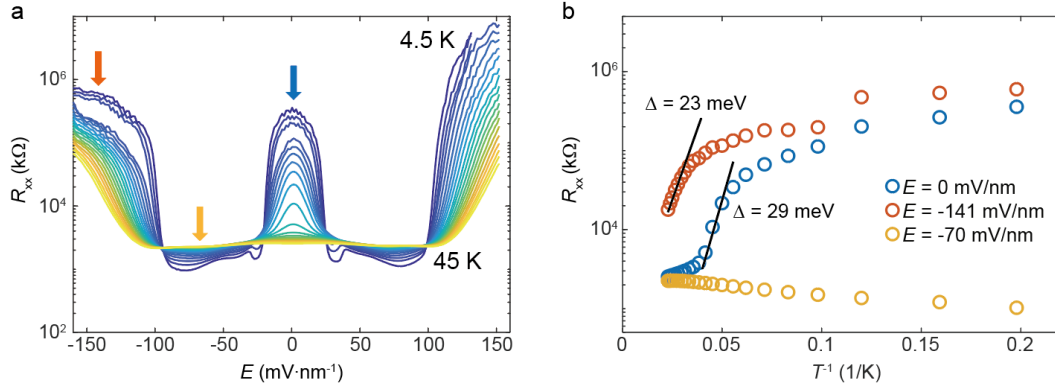


Figure S1 | Temperature-dependent correlated and band insulating states. **a**, Temperature-dependent R_{xx} measured at $n = 0$ from 4.5 K to 45 K. **b**, R_{xx} versus $1/T$ plot at different E extracted from the corresponding arrows in **a**. At zero E (blue) and high E (orange) regions, the R_{xx} increases with decreasing temperature, exhibiting insulating behavior at low temperatures. Between these two insulating phases (yellow), the R_{xx} decreases with decreasing temperature, indicating typical metallic behavior. We extract the transport gap Δ by using the formula $R_{xx} \propto e^{-\Delta/2kBT}$, as shown by the black line in **b**. At high temperatures ($T > 28$ K) and zero electric field, the slope dramatically decreases, indicating that the gap value decreases with increasing temperature. This observation is consistent with the previously observed correlated insulating states in tetralayer and pentalayer graphene^{1,2}.

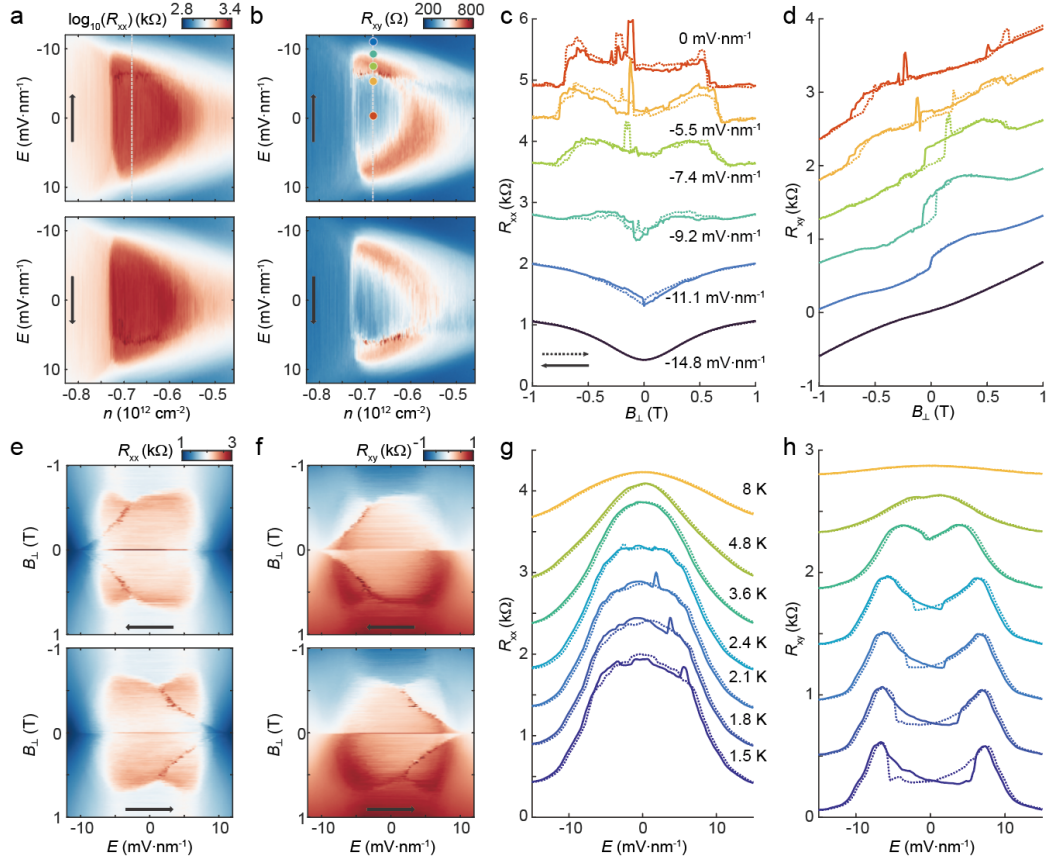


Figure S2 | Electric field and magnetic field control of multiferroic states. **a, b**, n and E dependent R_{xx} (**a**) and R_{xy} (**b**), the upper and lower panels represent results with forward and backward scanning of E , respectively. A small magnetic field $B_{\perp} = 50$ mT is added to stabilize the magnetic order. Abrupt changes in R_{xy} at around critical electric field $E_c = -6$ mV·nm⁻¹ (forward) and 6 mV·nm⁻¹ (backward) indicate that the magnetic order can be reversed by the electric field. **c, d**, Electric-field-dependent magnetic hysteresis of R_{xx} (**c**) and R_{xy} (**d**) recorded at $n = -0.68 \times 10^{12}$ ·cm⁻². The location of each curve in n - E parameter space is marked by dots in **b** with corresponding color, except for the black ones at $E = -14.8$ mV·nm⁻¹, which are out of the range in **b**. Dashed and solid curves represent the forward and backward scanning of B_{\perp} . The hysteresis behavior in R_{xy} reveals the existence of orbital magnetization, which can be further tuned by the electric field due to the tunable Berry curvature. **e, f**, B_{\perp} and E dependent R_{xx} (**e**) and R_{xy} (**f**) at $n = -0.68 \times 10^{12}$ ·cm⁻², the upper and lower panels represent results with forward and backward scanning of E , respectively. The B_{\perp} dependent $2\Delta E_c$ indicates the coupling between E and magnetic ordering. **g, h**, Temperature-dependent E hysteresis of R_{xx} (**g**) and R_{xy} (**h**) at $n = -0.68 \times 10^{12}$ ·cm⁻². The butterfly-like hysteresis behavior is weakened with elevated temperature up to 3.6 K and eventually vanishes at 4.8 K, suggesting a multiferroic transition temperature $T > 3.6$ K. All data in this figure are acquired at 1 K except for the temperature-dependent measurement.

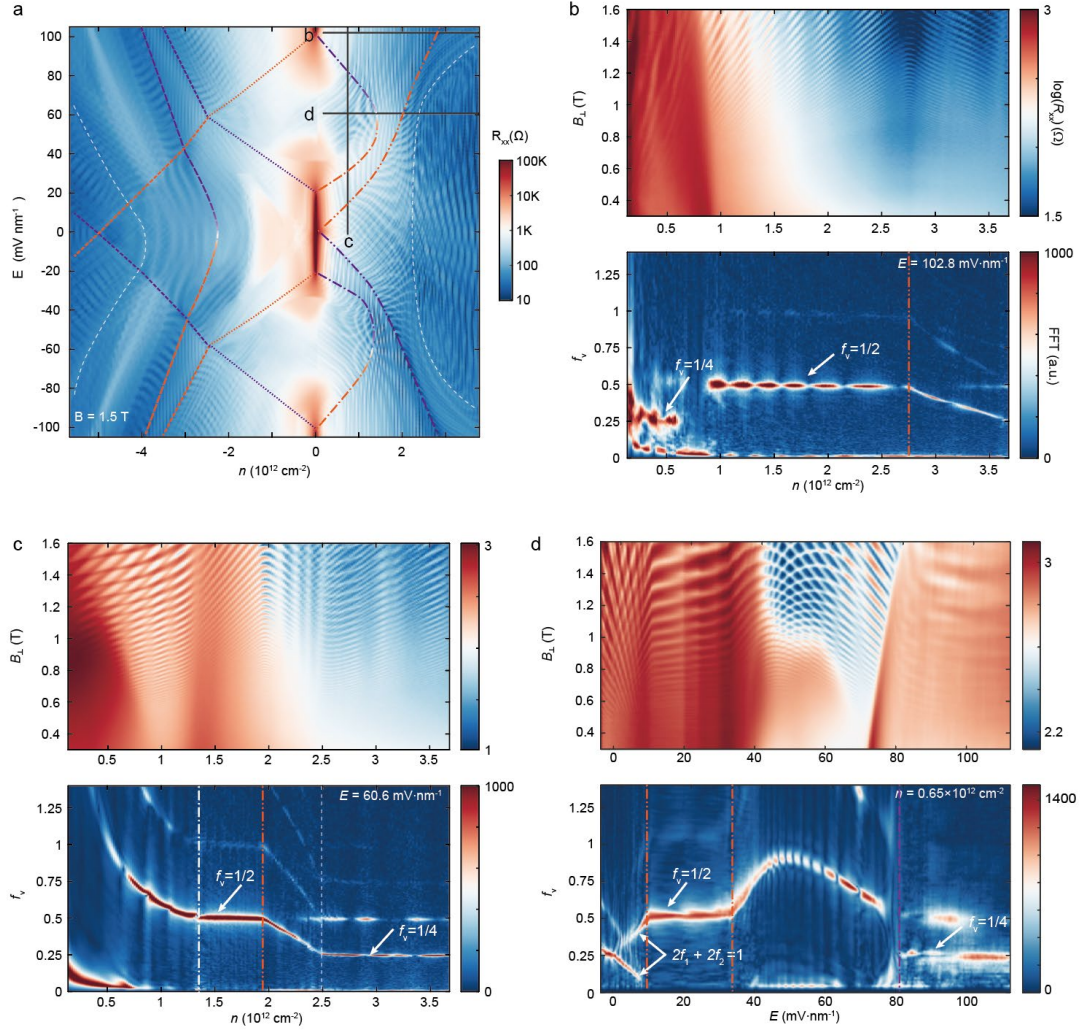


Figure S3 | Fermiology at electron-doped side. **a**, Longitudinal resistance vs n and E at 1.5 T (same as Fig. 2a). The phase boundaries as shown in **a** are also marked in **b**, **c**, and **d**. **b**, **c**, and **d**, Quantum oscillations and their FFT results acquired at $E = 102.8, 60.6 \text{ mV nm}^{-1}$, and $n = -0.65 \times 10^{12} \text{ cm}^{-2}$, respectively. The location of the linecuts is marked by black solid lines in **a**.

In **b**, we show that doping the band insulator will first lead to a Fermi surface with a four-fold degeneracy, which can be explained by either a simple full metal or a two-fold degenerate nematic half metal, which were observed at low carrier density area in trilayer rhombohedral graphene³. Increasing the doping level can tune the system into a half-metal state with a two-fold degeneracy and then transfer to a partially isospin (flavor) polarized state with a violation of the sum rule. As shown in Fig. 2g, this partially flavor polarized stems from the involvement of the conduction band bottom in flavor B. In **c**, we show a quantum oscillation result of doping the band overlapped semimetallic regime located between the band insulator and correlated insulator. Here, the semimetallic regime shows partially isospin polarized features, suggesting the complex Fermi surface nature in the band overlapped semimetal region, and further transfer

to a half metal state with the increasing doping level. Keeping increasing the carrier density can lead to a half-metal to full metal transition with a partially isospin polarized transition state. In **d**, constant carrier density quantum oscillation results show a clear *E-dependent* band evolution. At zero electric field, the Fermi surface is formed by a four-fold degenerate full metal state. Increasing the electric field elevates the conduction band edge energy in one of the flavors (*i.e.*, flavor B as we showed in Fig. 2), leading to an immediate splitting of the four-fold degenerated band into a majority and a minority two-fold degenerated bands. When $E > 10 \text{ mV}\cdot\text{nm}^{-1}$, an electric field triggered Lifshitz transition appears, where the minority Fermi surface disappears and transitions to a half-metal state. Keep increasing carrier density tunes the system into the partially isospin polarized and four-fold degenerated metallic states as we discussed in **b** and **c**.

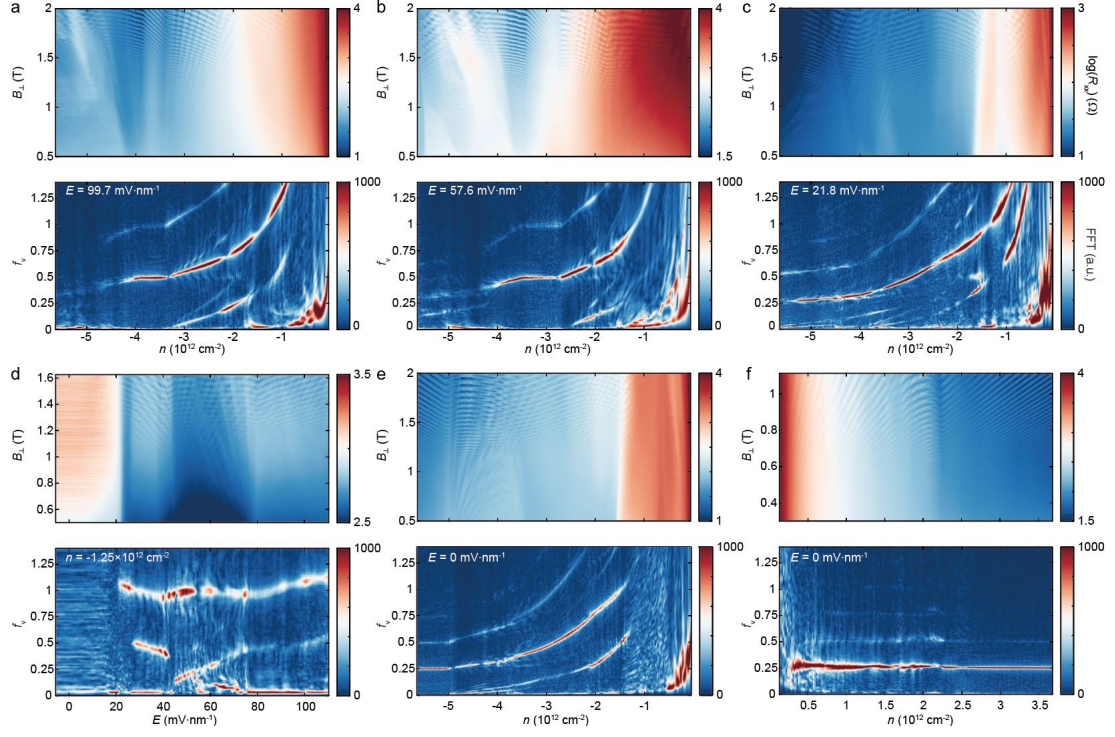


Figure S4 | Raw data of the quantum oscillation and the corresponding FFT results. a to f, Quantum oscillation and their FFT results as shown in Fig. 2. a, b, c, and d correspond to the Figs. 2b, c, d, and f, respectively. e and f correspond to the hole-doped and electron-doped region in Fig. 2e

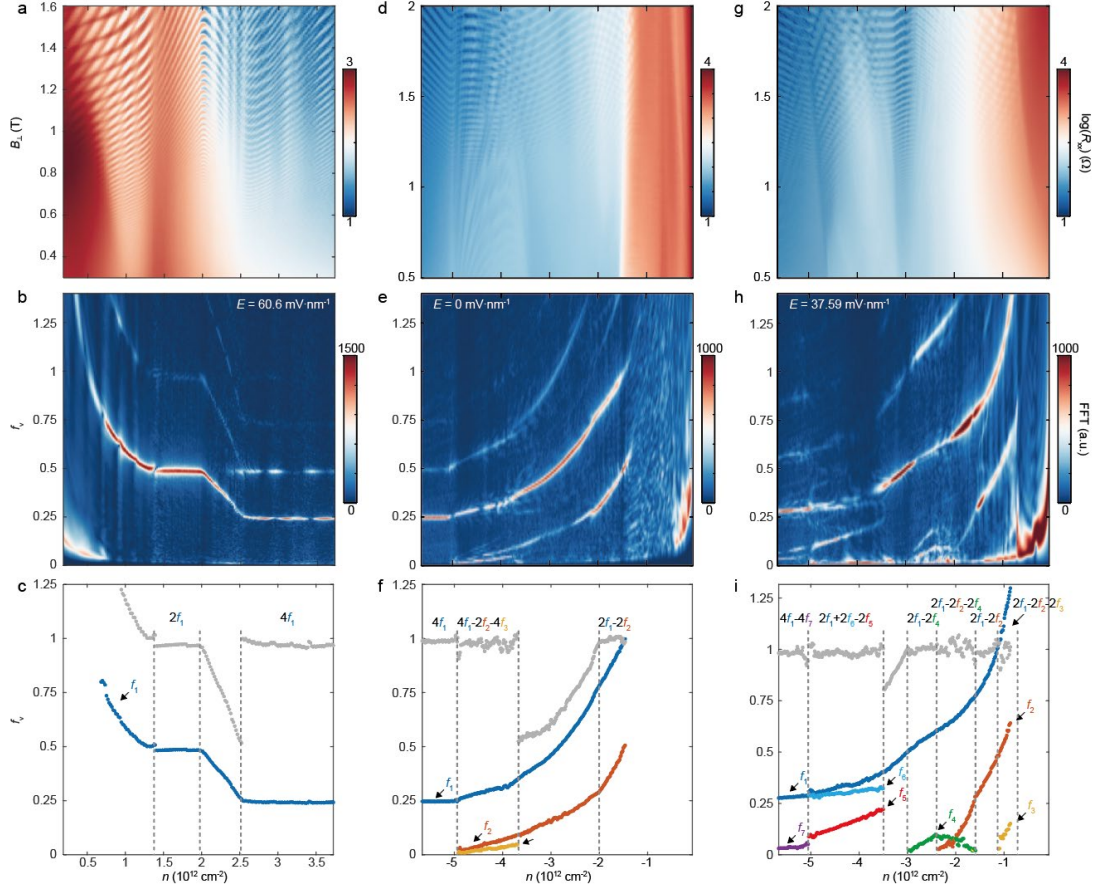


Figure S5 | Sum rule discussion of quantum oscillation results and their violation at partially flavor polarized states. **a** to **c**, Quantum oscillation (**a**), FFT results (**b**), and extracted frequency peaks and their sum rule illustration (**c**) performed at $E = 60.6 \text{ mV}\cdot\text{nm}^{-1}$ linecut at electron side. **d** to **f**, Quantum oscillation (**d**), FFT results (**e**), and extracted frequency peaks and their sum rule illustration (**f**) performed at $E = 0 \text{ mV}\cdot\text{nm}^{-1}$ linecut at hole side. **g** to **i**, Quantum oscillation (**g**), FFT results (**h**), and extracted frequency peaks and their sum rule illustration (**i**) performed at $E = 37.59 \text{ mV}\cdot\text{nm}^{-1}$ linecut. In extracted results **c**, **f**, and **i**, the extracted frequency peaks are colorfully marked, and their sum rule results are calculated and shown in gray dots.

The sum for normalized frequency (f_v) should, in principle, follow the sum rule $\sum_i s_i k_i f_i = 1$, where s can be either -1 or 1, representing electron- or hole-like Fermi surface, and k indicates the degeneracy of the Fermi surface. In **c**, we show two representative half-metal and full metal phases on the electron-doped side with a simple two-fold ($2f_1 = 1$) and four-fold degenerated ($4f_1 = 1$) enclosed Fermi surface. However, we noticed some areas showing a violation of sum rules in connection with these phases. These phases were commonly observed in other rhombohedral multilayer graphene system^{4,5}, which is usually observed between symmetry-breaking phases and therefore attributed to partially flavor polarization. A possible explanation of these violations is that these transition phases always involve multiple small Fermi surfaces

with high degeneracy and high effective mass⁶, which is difficult to resolve by quantum oscillation measurements.

In **f**, we discuss the Fermi surface evolution versus carrier density at the $E = 0$ linecut at hole hole-doped side. Doping the zero E CI state first goes to (multiferroic) orbital magnetism phases, where we observed no quantum oscillation. Recent theoretical work predicted the missing quantum oscillation due to the unique Fermi surface geometry in the orbital magnetism regime in the multilayer rhombohedral graphene system, which might be the possible explanation for our missing quantum oscillation⁷. Across the orbital magnetism triangle region, the quantum oscillation signal appears with the sum rule $2f_1 - 2f_2 = 1$, indicating a typical half-metallic hole-doped annular Fermi surface. Increasing the carrier density pushes the system across to a partially flavor polarized state that violates the sum rule and then transits to a complex multiple Fermi surface region when $|n| > 3.6 \times 10^{12} \cdot \text{cm}^{-2}$, before the simple full metallic state ($4f_1 = 1$). In this region, we found the sum rule $4f_1 - 2f_2 - 4f_3 = 1$ that can be partially understood with a similar band picture in Fig. 2i. At this high carrier density, both flavor A and flavor B are involved in the Fermi surface, leading to a four-fold degenerate outermost band $4f_1$. Instead of a four-fold degenerate electron-like Fermi surface $4f_2$, the inner Fermi surface shows a more complex structure with a two-fold degenerate $2f_2$ and a four-fold degenerate $4f_3$, which cannot be simply explained by single particle band structure and points to a possible nematic ordering³.

In **i**, we discuss the Fermi surface evolution versus carrier density at $E = 37.59 \text{ mV} \cdot \text{nm}^{-1}$ linecut across the SC1 state at hole hole-doped side. With low carrier density $|n| < 1.6 \times 10^{12} \cdot \text{cm}^{-2}$, the quantum oscillation sum rule can be understood from a single particle picture as we illustrated in Fig. 2i. The system starts with an electron-hole overlapped semimetallic region indicated by sum rule $2f_1 - 2f_2 - 2f_3 = 1$, which can be explained by a combination of majority annular hole-like Fermi surface ($2f_1 - 2f_2$) with a minority electron-like enclosed Fermi surface ($2f_3$). With the increasing hole doping, the minority electron-like pocket keeps getting smaller and eventually disappears, turning the system into a half-metallic state with a two-fold degenerate annular Fermi surface ($2f_1 - 2f_2 = 1$).

With the increasing hole doping, the emergent electron Fermi surface appears with a two-fold degeneracy, and the whole Fermi surface can be described by the sum rule $2f_1 - 2f_2 - 2f_4 = 1$. The relative area ratio between f_2 and f_4 shows a crossover, and the originally minority band f_4 persists even after the f_4 disappears ($2f_1 - 2f_4 = 1$), indicating a Lifshitz transition between the f_2 and f_4 bands during the carrier density increase. Passing through a partially flavor polarized state, two additional Fermi surface emerges as f_5 and f_5 with the sum rule $2f_1 + 2f_6 - 2f_5 = 1$ when $|n| > 3.5 \times 10^{12} \cdot \text{cm}^{-2}$, which is consistent with the band diagram we have shown in Fig. 2i. Here the Fermi level in flavor A has across the bottom of Mexican hat like band structure ($2f_1$) while still keeps in the other flavor B band with an annular Fermi surface ($2f_6 - 2f_5$). When $|n| > 5 \times 10^{12} \cdot \text{cm}^{-2}$, the Fermi surface transfers into a full metallic annular structure with four-

fold degeneracy.

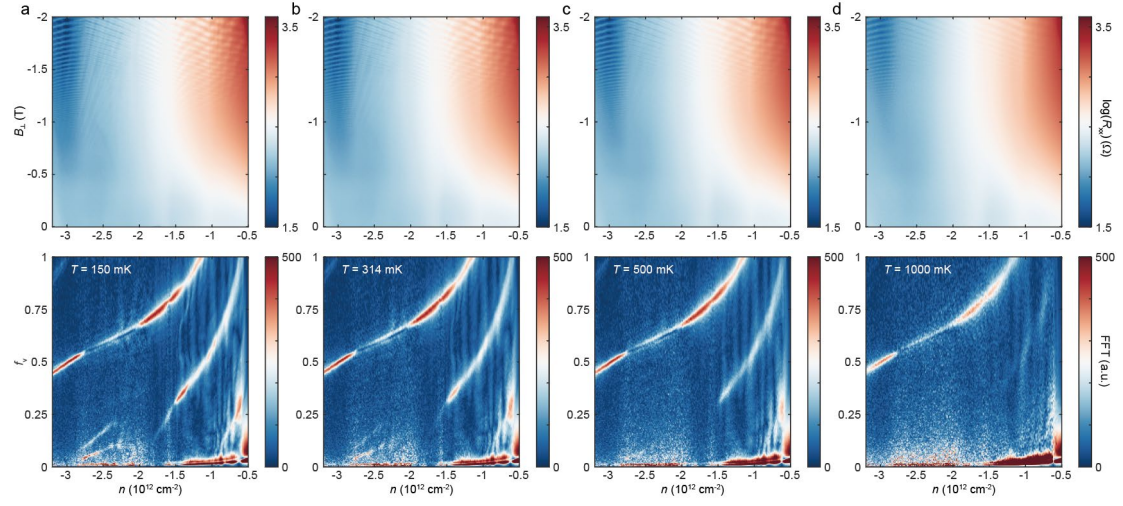


Figure S6 | Temperature-dependent quantum oscillation near the SC1 region. **a to d,** Quantum oscillation and their FFT results performed along the $E = 41.6 \text{ mV}\cdot\text{nm}^{-1}$ linecut at the hole doping region at $T = 150, 314, 500,$ and 1000 mK , respectively. The peak intensity of the emergent Fermi surfaces between $1.5 \times 10^{12}\cdot\text{cm}^{-2} < |n| < 33 \times 10^{12}\cdot\text{cm}^{-2}$ gradually suppressed and eventually faded out with the elevated temperature.

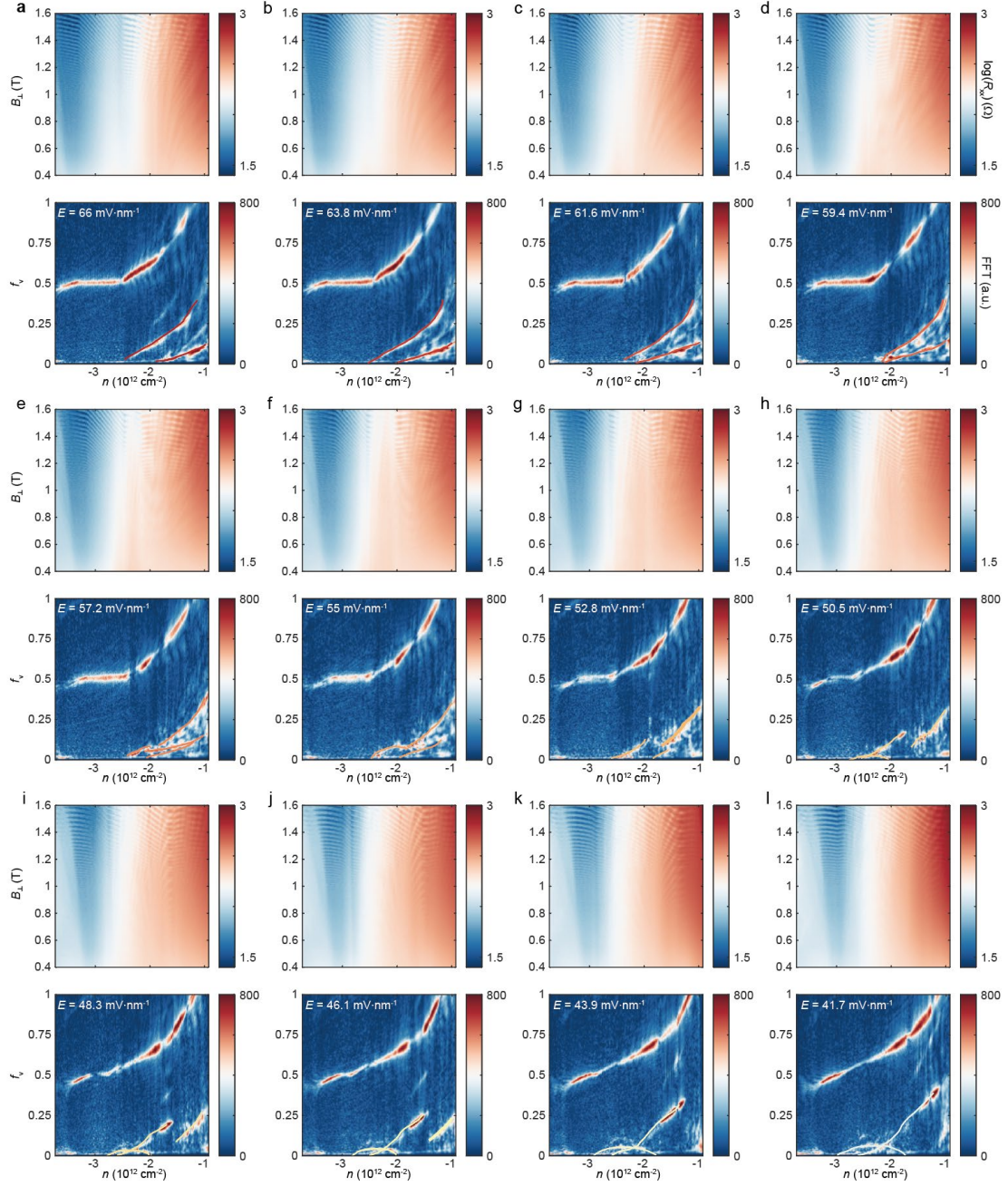


Figure S7 | Quantum oscillation data near SC1 (part I). **a to l**, Raw quantum oscillation data and their FFT results near the SC1 region with E ranging from 66 to 41.7 $\text{mV}\cdot\text{nm}^{-1}$. The low-frequency peaks that were shown in Fig. 3d are sketched and overlapped on the FFT results by curves with the same color.

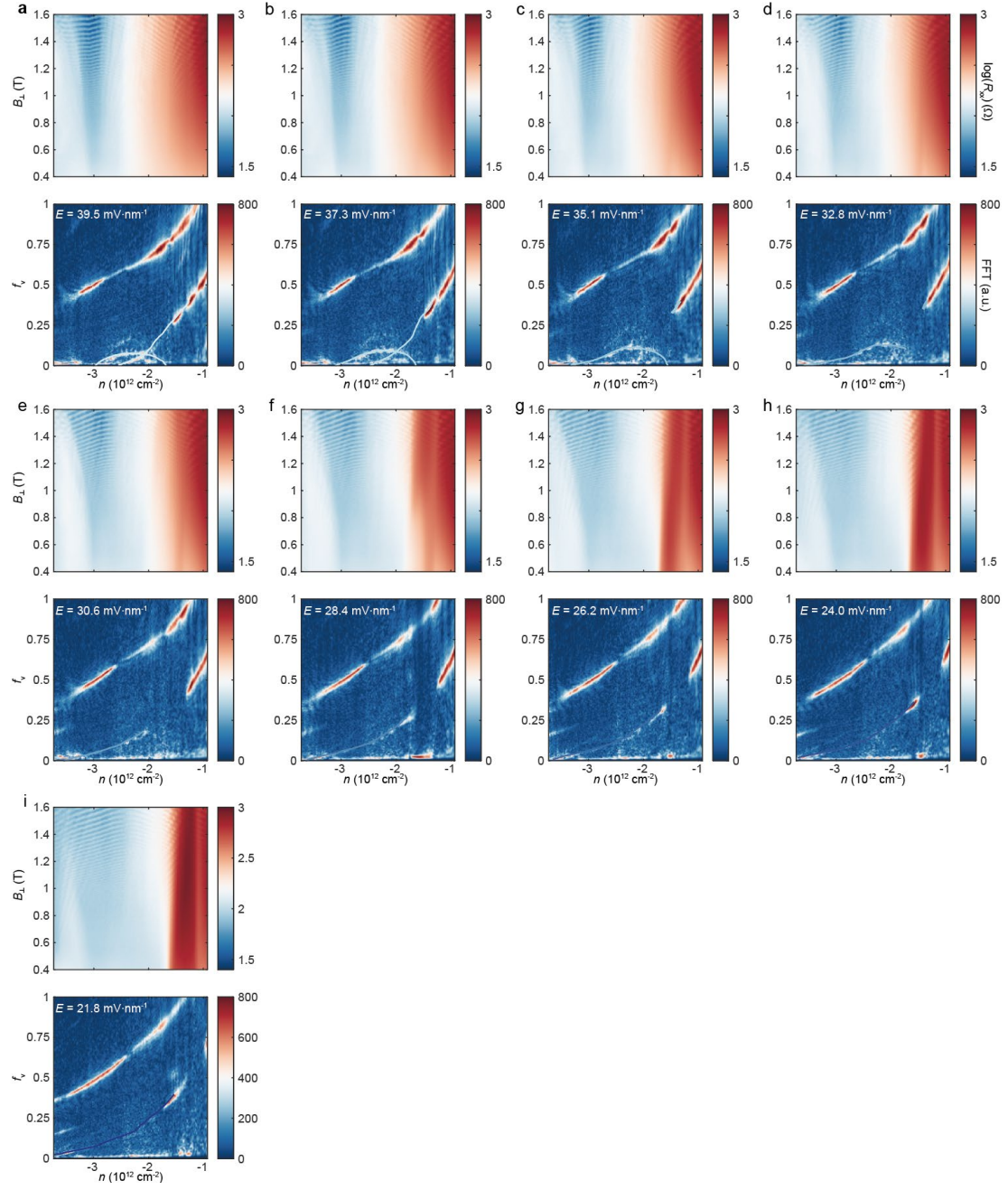


Figure S8 | Quantum oscillation data near SC1 (part II). a to i, Raw quantum oscillation data and their FFT results near the SC1 region with E ranging from 39.5 to 21.8 mV·nm⁻¹. The low-frequency peaks are sketched by curves with the same color as were shown in Fig. 3d.

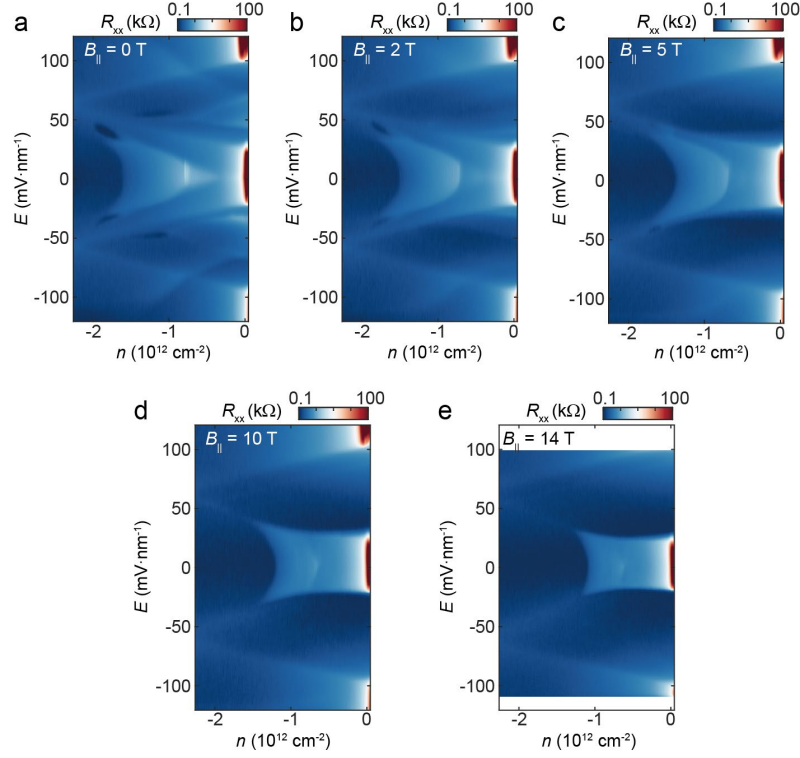


Figure S9 | In-plane magnetic field dependent evolution of R_{xx} - n - E mapping. **a** to **e**, Longitudinal resistance vs n and E under different in-plane magnetic fields at 0, 2, 5, 10, and 14 T, respectively. At 0 T, we observe both SC1 and SC2 states. Increasing the in-plane magnetic field to 2 T can significantly suppress the SC2 while the SC1 persists (**b**), consistent with the result in Fig. 3g. Increasing the magnetic field can further shrink the SC1 state at 5 T (**c**), and eventually close the SC1 state as we show in **d**. We noticed that the in-plane magnetic field can strongly suppress the triangular orbital magnetism region. This phenomenon can be understood by the competing ground state energy under the in-plane magnetic field. Since the valley/orbital momentum should have little contribution to the in-plane magnetic field, the spin-related Zeeman energy should dominate the phase competition. Therefore, the suppression of the orbital magnetism regime under in-plane magnetic field is consistent with their valley-polarized nature.

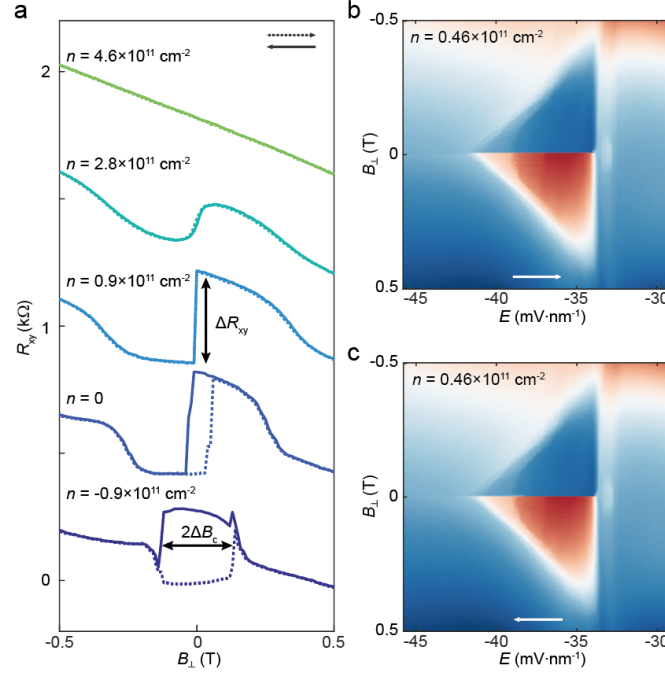


Figure S10 | Carrier density dependent ferromagnetic-paramagnetic transition. a, Carrier density dependent magnetic hysteresis R_{xy} recorded at different n at $E = -36 \text{ mV} \cdot \text{nm}^{-1}$. Dashed and solid curves represent the forward and backward scanning of B_{\perp} . Hall resistance difference ΔR_{xy} and coercive field $2\Delta B_c$ are defined by arrows. **b, c,** Color-coded B_{\perp} -dependent E hysteresis scanning of the R_{xy} at $n = 0.46 \times 10^{11} \cdot \text{cm}^{-2}$. White arrows in **e** to **f** represent the direction of scanning.

At $n = -0.9 \times 10^{11} \cdot \text{cm}^{-2}$, the R_{xy} signal shows a significant hysteresis Hall response with the sweeping of B_{\perp} , indicating the existence of ferromagnetism in this comet-like region with a coercive field $2\Delta B_c \sim 0.3 \text{ T}$ and Hall resistance difference $\Delta R_{xy} = \sim 300 \Omega$. Increasing the carrier density to $n = 0$ increases the ΔR_{xy} to $\sim 400 \Omega$. This can be understood with the orbital magnetism picture that magnetism is directly connected to Berry curvature, which is always concentrated near the band edge in the rhombohedral graphene system^{8,9}. While the ΔR_{xy} persists up to $n = 2.8 \times 10^{11} \cdot \text{cm}^{-2}$, the strongly suppressed and eventually vanished coercive field suggests a continuous magnetic phase transition from ferromagnetism to paramagnetism. A possible explanation for this transition is that the increased carrier density will involve more dispersive carriers in the conduction band, leading to a competing state between kinetic energy and condensed Berry curvature. Based on Stoner criteria, the increased kinetic energy can suppress the magnetic momentum ordering, leading to paramagnetic behavior.

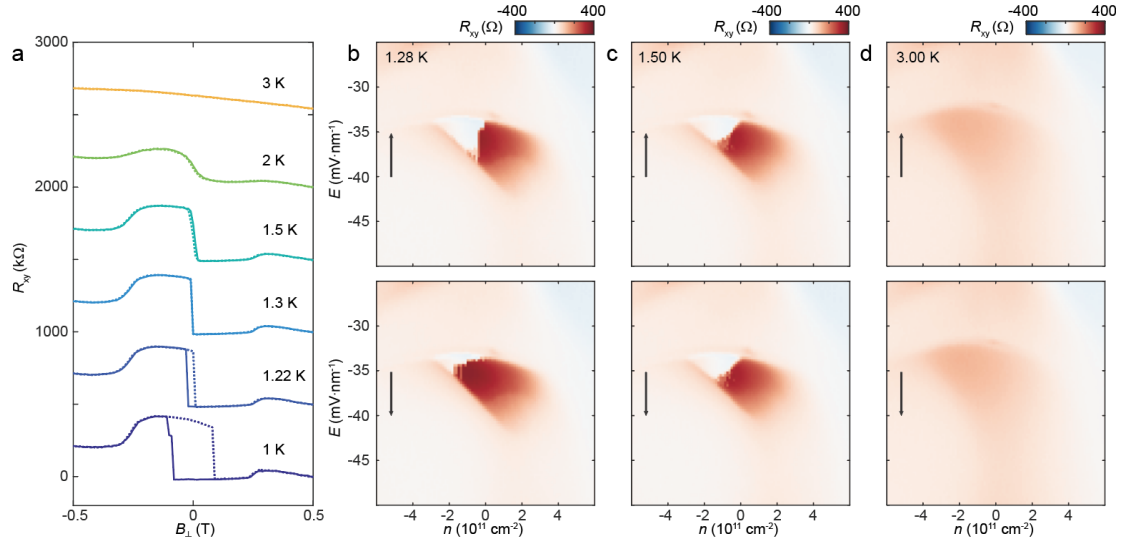


Figure S11 | Temperature dependency of the finite-field multiferroicity. **a, b,** Temperature-dependent magnetic hysteresis of R_{xy} at $n = -0.9 \times 10^{11} \cdot \text{cm}^{-2}$, $E = -36 \text{ mV} \cdot \text{nm}^{-1}$. The result shows a vanished coercive field at 1.3 K, but sharp magnetization switches persist. At 2 K, the magnetization switch becomes soft, indicating a ferromagnetic to paramagnetic transition at this temperature. The signal of magnetization switches fully vanished at 3 K, suggesting that the orbital magnetism is fully suppressed at the elevated temperature. **b, c, d,** Color-coded temperature-dependent E hysteresis of R_{xy} measurements at 1.28, 1.5, and 3 K, respectively. Upper (lower) panels were acquired by sweeping E backward (forward) along the arrow direction in each figure. At 1.28 K, we can still observe the E -hysteresis in the lower doping region, which vanishes at 1.5 K. However, the Hall signal is still significant at 1.5 K and eventually fades out at 3 K, which is consistent with the magnetic hysteresis measurements in **a**. These temperature-dependent measurements reveal a two-step transition. With the elevated temperature, the ferroic ordering of both orbital magnetism and valley polarization is first suppressed and disappears at 1.5 K. Raising the temperature can suppress the orbital magnetism and make it fully vanish at 3 K.

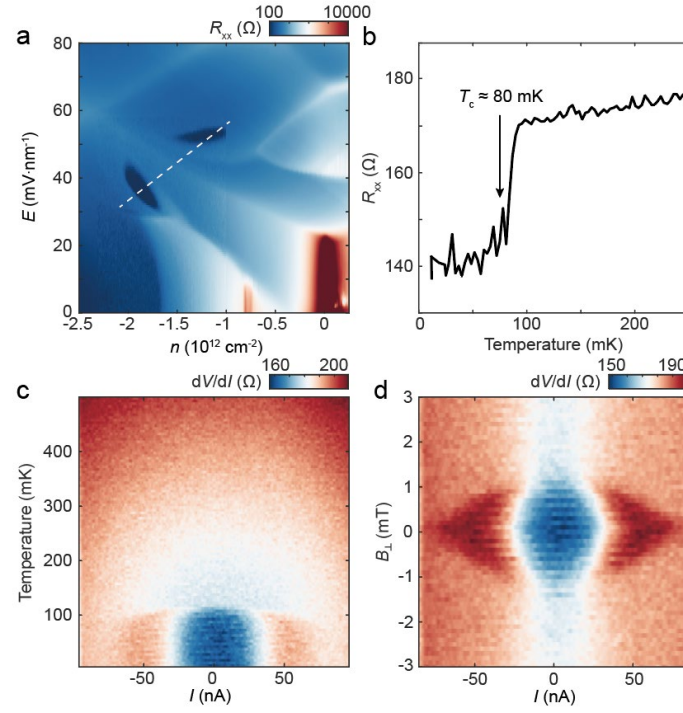


Figure S12 | Characterization of SC2 and phase connection between superconductivity and multiferroic. a, Zoomed-in longitudinal resistance vs n and E . The white dashed line indicates the location of the linecut shown in Fig. 3g. **b,** Temperature-dependent longitudinal resistance of SC2 states. A dramatic increase in resistance appears when the temperature is elevated to the $T_c \sim 80 \text{ mK}$. **c, d,** Temperature and out-of-plane magnetic field dependent dV/dI measurements of SC2. The disappearance of non-linear dV/dI features reveals a similar transition temperature as we showed in **b**, and a critical out-of-plane magnetic field of $\sim 1 \text{ mT}$.

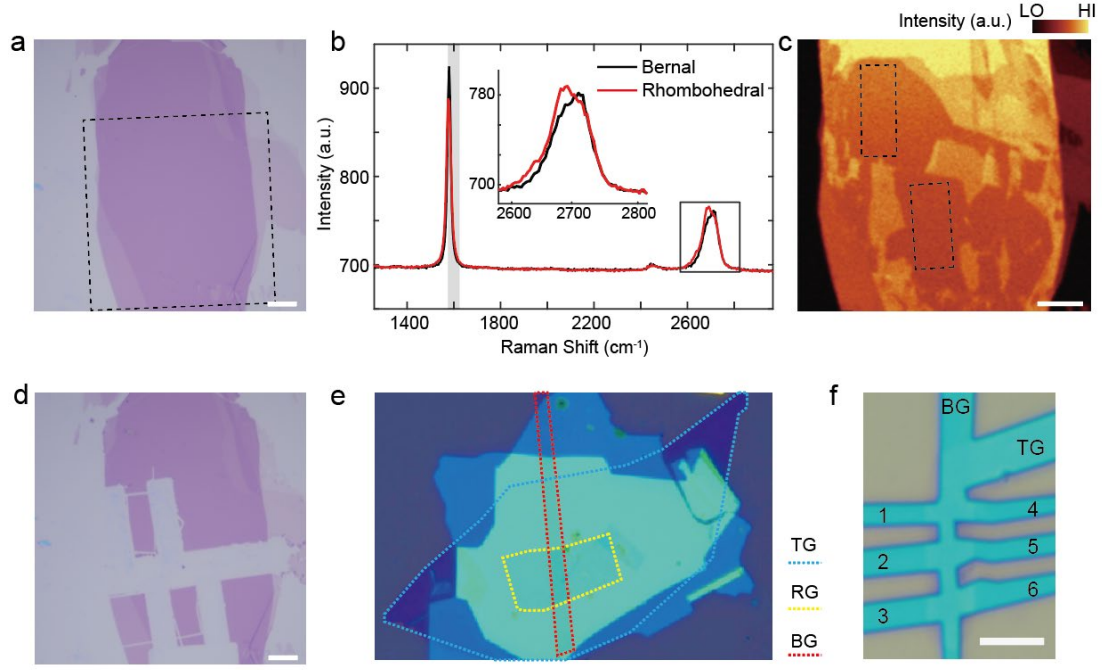


Figure S13 | Determination, isolation, and stacking of rhombohedral graphene. **a**, Optical microscope image of hexalayer graphene used for device fabrication. The thickness of the graphene layer is recognized by extracting the optical contrast between the SiO₂/Si substrate and the graphene layers. **b**, Typical large range Raman spectra of rhombohedral and Bernal hexalayer graphene, including both 2D band ($\sim 2700 \text{ cm}^{-1}$) and G band ($\sim 1600 \text{ cm}^{-1}$)¹⁰. While we still use the shape of a 2D band for the final determination of rhombohedral stacking order, we find that integrating half of the G band and mapping it out in real space provides a higher contrast between different domains. **c**, The Raman mapping extracted from integrating the G band (gray shadow in **b**). Black dashed boxes show the rhombohedral area that we isolated later by the AFM lithography method. **d**, The same flake as we have shown in **a** after AFM lithography. **e**, Optical microscope image of the final stack, where the top graphite gate (TG), rhombohedral graphene (RG), and bottom gate (BG) are highlighted by blue, yellow, and red dashed lines, respectively. **f**, Optical image after Hall bar device fabrication. Pins for electric transport measurements were marked by numbers 1 to 6.

Reference

1. Han, T. *et al.* Correlated insulator and Chern insulators in pentalayer rhombohedral-stacked graphene. *Nat. Nanotechnol.* **19**, 181–187 (2024).
2. Liu, K. *et al.* Spontaneous broken-symmetry insulator and metals in tetralayer rhombohedral graphene. *Nat. Nanotechnol.* **19**, 188–195 (2024).
3. Holleis, L. *et al.* Nematicity and orbital depairing in superconducting Bernal bilayer graphene. *Nat. Phys.* **21**, 444–450 (2025).
4. Zhou, H. *et al.* Half- and quarter-metals in rhombohedral trilayer graphene. *Nature* **598**, 429–433 (2021).
5. Li, C. *et al.* Tunable superconductivity in electron- and hole-doped Bernal bilayer graphene. *Nature* **631**, 300–306 (2024).
6. Huang, C. *et al.* Spin and orbital metallic magnetism in rhombohedral trilayer graphene. *Phys. Rev. B* **107**, L121405 (2023).
7. Li, M. *et al.* Fermi lune and transdimensional orbital magnetism in rhombohedral multilayer graphene. Preprint at <https://doi.org/10.48550/arXiv.2505.05414> (2025).
8. Zhang, F., Sahu, B., Min, H. & MacDonald, A. H. Band structure of ABC-stacked graphene trilayers. *Phys. Rev. B* **82**, 035409 (2010).
9. Zhang, F., Jung, J., Fiete, G. A., Niu, Q. & MacDonald, A. H. Spontaneous Quantum Hall States in Chirally Stacked Few-Layer Graphene Systems. *Phys. Rev. Lett.* **106**, 156801 (2011).
10. Lui, C. H. *et al.* Imaging Stacking Order in Few-Layer Graphene. *Nano Lett.* **11**, 164–169 (2011).